Excellent self-cleaning, ultrawideband-absorption, and rapid-heat-dissipation of magnetic hybrid foams from a facile one-step annealing route

Yangbing Chen,[†] Ran Ji,[†] Xuan Chen,[†] Peiwen Wang,[†] Huiming Ye,[†] Guoxiu Tong,[*][†] Xiaojuan Wang, [†] Wenhua Wu[†]

[†]*College of Chemistry and Material Sciences, Key Laboratory of the Ministry of Education for Advanced Catalysis Materials, Zhejiang Normal University, Jinhua 321004, China.*

* **Corresponding Authors:** E-mail: tonggx@zjnu.cn (G.X. Tong). Tel.: +86-579-82282269; Fax: +86-579-82282269.

1. Experiment section

1.1 Characterization

ZEISS GeminiSEM 300 scanning electron microscope (SEM, 10 kV) and a Horiba EX-250 energy dispersive X-ray spectrometer (EDS) connected with it were applied to analyze the surface morphology, element content and distribution of the MHFs. A JEM-2100F transmission electron microscope (TEM, 200 kV) was used to further confirm the microstructure of the MHFs. A D/MAX-IIIA X-ray diffractometer (XRD) with X-ray ($\lambda = 0.15418$ nm, came from Cu Kα) as the radiation source was employed to record XRD patterns for the phase analysis. The working voltage, working current, and scanning speed were 40.0 kV, 40.0 mA, 6 °/min, respectively. The crystallite sizes and the microstrain level were obtained by analyzing and calculating using Jade 6.

The graphitization degree analysis of carbon was executed on a Renishaw RM10000 Raman spectrometer. The oxidation states of surface elements are assessed in the samples using a ESCALAB250 X-ray photoelectron spectroscopy (XPS). To obtain the Brunauer–Emmett–Teller (BET) specific surface area (S_{BET}), the N_2 adsorption/desorption isotherm was done on an Autosorb iQ instrument (Quantachrome, Florida, USA), and the sample was outgassed under vacuum at 160 °C for 8 h.

1.2 Measurement of conductivity, EM parameters, and heat conductance.

Measurement of magnetic performance: The magnetic performance of the MHFs at room temperature was measured on a vibrating sample magnetometer (Model 7404, LakeShore, USA).

Measurement of electrical/thermal conductivities: To test the electrical conductivity and thermal conductivity of the as-obtained the MHFs/silicone films, magnetic foams were uniformly dispersed into the silicone oils with a 30 wt.% load. Afterward, the above mixture is solidified into circular silicone film in a mold and the as-obtained circular the MHFs/silicone films is 30.0 mm in diameter and about 0.50 mm in thickness.

The **electrical conductivity** of the MHFs/silicone films were tested on a four-point probe instrument (RTS-9 model, Guangzhou, China).

The **thermal conductivity** of the MHFs/silicone films were tested on a Hot Disk thermal constant analyzer (TPS 2500; Uppsala; Sweden), which meets the ISO

Standard 22007e2. When performing a measurement, a plane Hot Disk sensor of 5465 is fitted between two pieces of the MHFs/silicone films, each one with a plane surface facing the sensor which is used both as a heat source and as a dynamic temperature sensor. By running an electrical current, the temperature of the sensor increases, and the resistance (temperature) increase as a function of time was recorded at the same time to obtain the thermal conductivity. All measurements were carried out at room temperature and the average value of three repeated tests was determined.

Measurement of EM parameters: The as-obtained MHFs were mixed uniformly with molten paraffin in a load (10~50 wt.%), and the standard toroidal-shaped specimens were prepared with a mold. The thickness, outer diameter, and inner diameter of the standardized specimens were ca. 3.5 mm, 7.0 mm, and 3.04 mm, respectively. With the coaxial line method adopted, the permeability ($\mu_r = \mu' - j\mu''$) and permittivity ($\varepsilon_r = \varepsilon' - j\varepsilon''$) were measured using a Keysight N5230A vector network analyzer. Reflection loss (*RL*) generally representing the EMWAPs are computed by the equation: $RL = 20\log\left|\dfrac{\sqrt{\mu_r/\varepsilon_r}\,\tanh[j(2\pi fd/c)\sqrt{\mu_r\varepsilon_r}]-1}{\sqrt{\mu_r/\varepsilon_r}\,\tanh[j(2\pi fd/c)\sqrt{\mu_r\varepsilon_r}]+1}\right|$, where *f, c,* and *d,* correspond to the frequency, light velocity under vacuum, sample thickness, respectively. The attenuation constant (*A*) and matching constant (*Z*) are computed based on the formula:

$A = \dfrac{\sqrt{2}\pi f}{c}\sqrt{(\mu''\varepsilon'' - \mu'\varepsilon') + \sqrt{(\mu'\varepsilon'' + \mu''\varepsilon')^2 + (\mu''\varepsilon'' - \mu'\varepsilon')^2}}$ and $Z = \left|\dfrac{Z_{in}}{Z_0}\right| = \left|\sqrt{\dfrac{\mu_r}{\varepsilon_r}}\,\tanh\left(j\dfrac{2\pi fd}{c}\sqrt{\mu_r\varepsilon_r}\right)\right|$, respectively.

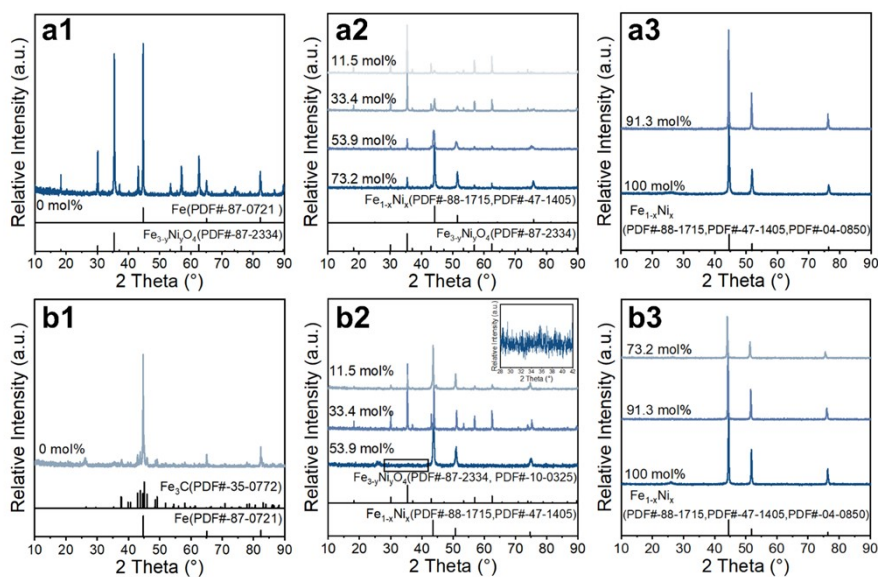**Figure S1** XRD patterns of the products formed under various [Ni^{2+}] (mol%) and diverse T_a: (a1–a3) T_a = 600 °C and (b1–b3) T_a = 800 °C.
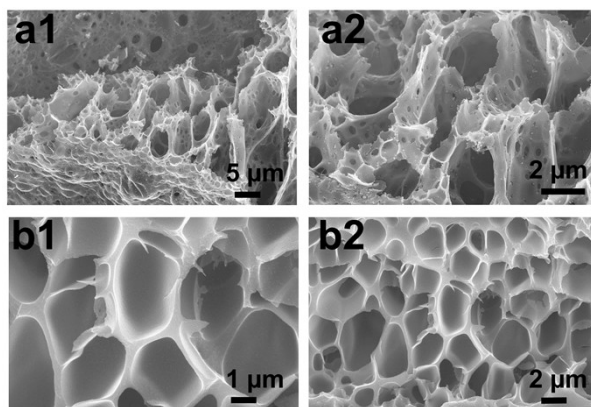

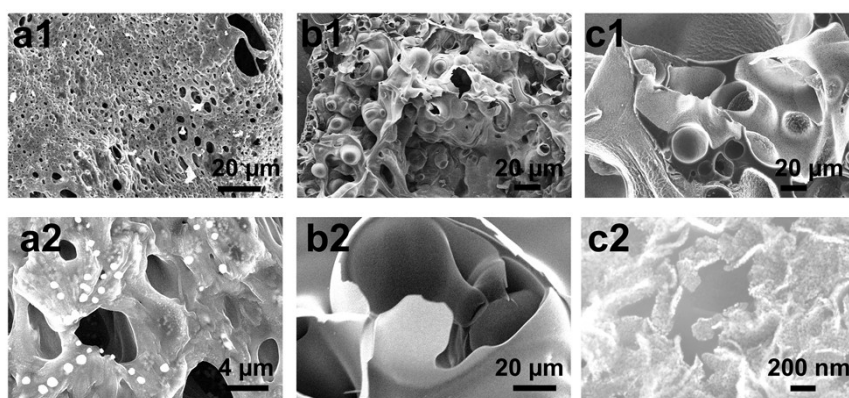**Figure S2** SEM images of the products formed under various nitrates: (a1–a2) $Co(NO_3)_2 \cdot 6H_2O$, (b1–b2) $Al(NO_3)_2 \cdot 9H_2O$

Figure S3 SEM images of the products formed under various nitrates: (a1–a2) $Cu(NO_3)_2 \cdot 3H_2O$, (b1–b2) $Ni(NO_3)_2 \cdot 6H_2O$, and (c1–c2) $Mg(NO_3)_2 \cdot 6H_2O$.

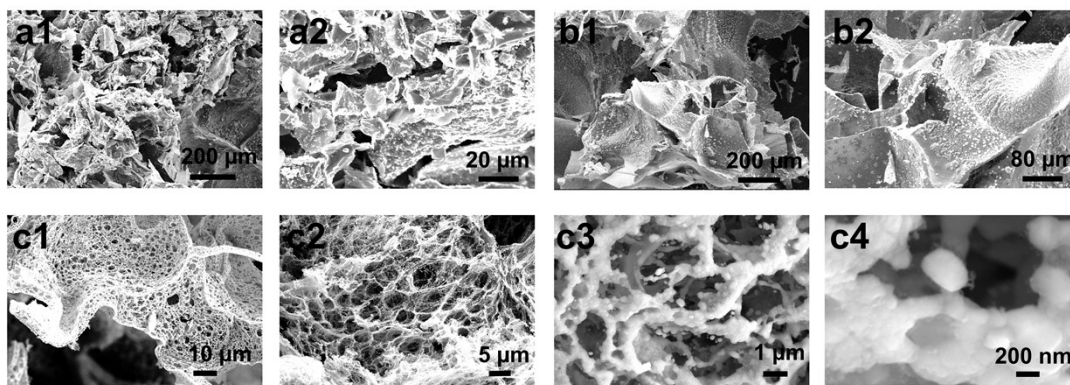**Figure S4** SEM images of the products formed using various salts: (a1–a2) $FeCl_3 \cdot 6H_2O$, (b1–b2) $Fe(Ac)_3 \cdot 4H_2O$, and (c1–c4) $Fe(NO_3)_3 \cdot 9H_2O$ and $Ni(NO_3)_2 \cdot 6H_2O$.
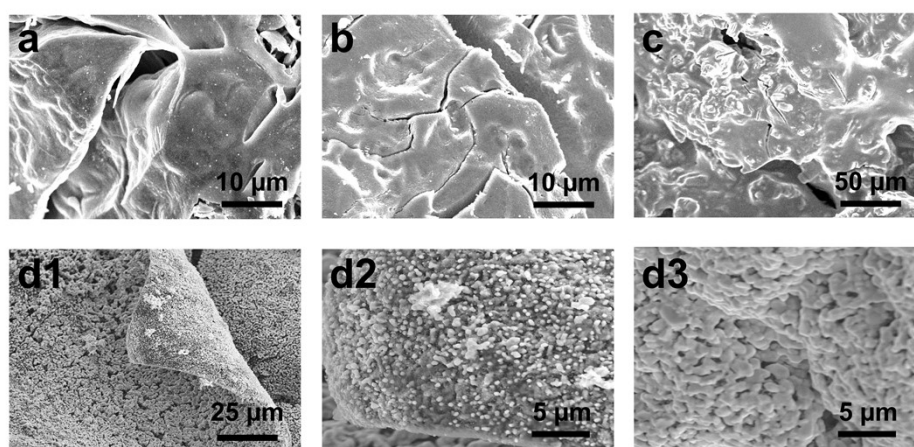

Figure S5 SEM images of the products formed using various surfactants as carbon sources: (a) polyacrylic acid (PAA), (b) PEG 2000, (c) sucrose, and (d1–d3) cetyltrimethyl ammonium bromide (CTAB).
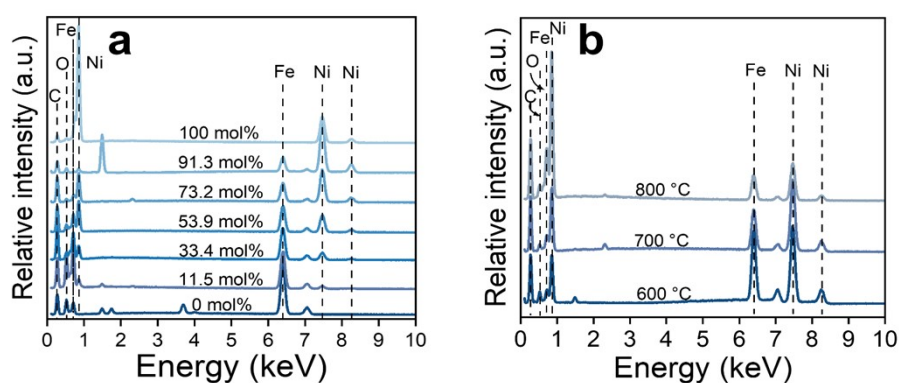

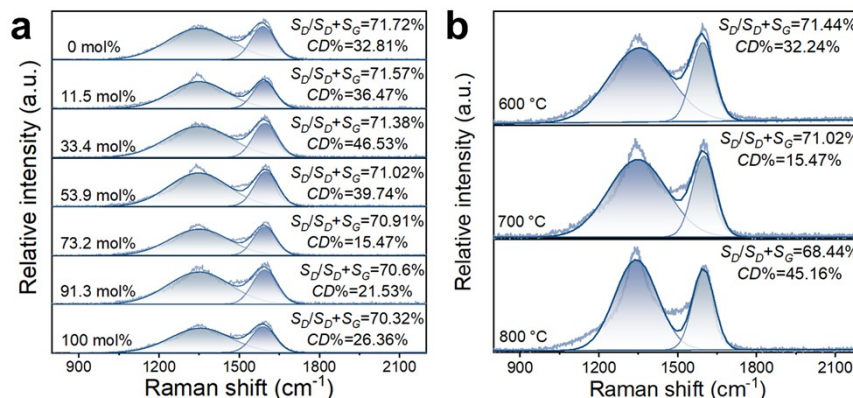**Figure S6** EDX spectra of the products formed under diverse (a) $[Ni^{2+}]$ (mol%) and (b) T_a.

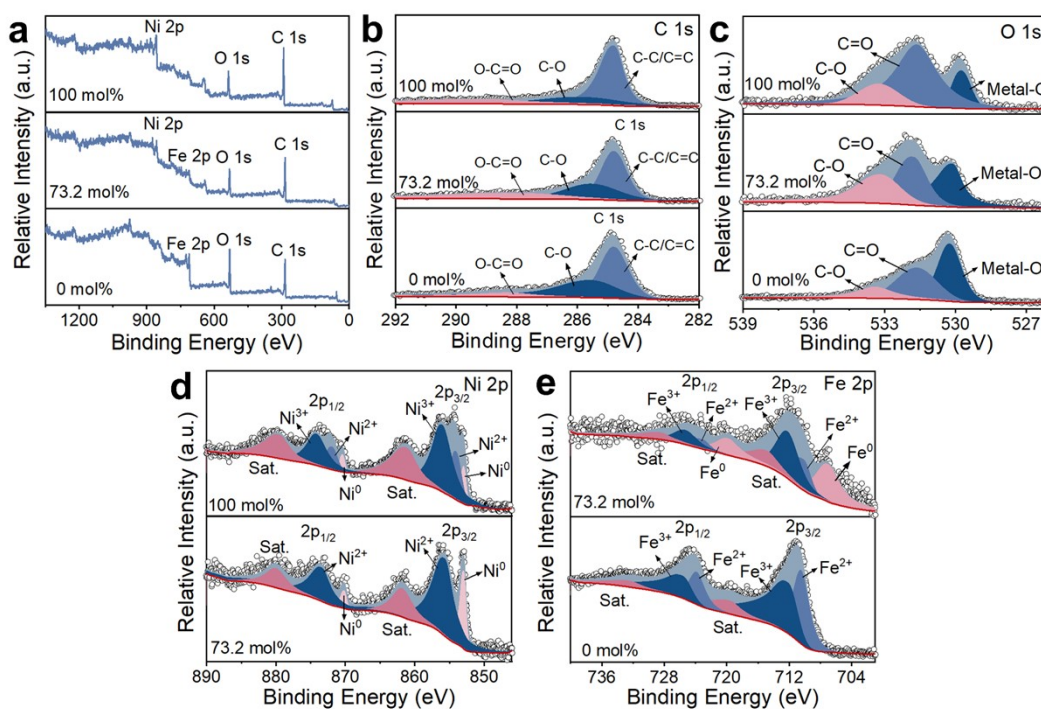**Figure S7** Raman spectra of the products formed under various (a) [Ni^{2+}] (mol%) and (b) T_a.

Figure S8 (a) XPS survey spectra and XPS fine spectra of (b) C 1s, (c) O 1s, (d) Ni 2p and (e) Fe 2p.

The elemental composition and their oxidation states in the MHFs were further revealed by X-ray photoelectron spectroscopy (XPS) further reveals the production of Fe/Fe$_3$O$_4$/C, Fe$_{1-x}$Ni$_x$/C, and Ni/C composites. The XPS survey spectra show that the coexistence of Fe, O, and C elements at [Ni^{2+}] = 0 mol%, Fe, O, Ni, and C at [Ni^{2+}] = 73.2 mol%, and Ni, O, and C at [Ni^{2+}] = 100 mol% (Figure S8a), which is in accord with EDX data (Figure 1c and Figure S6a). Looking at the C 1s spectra for the three products (Figure S8b), there are three fitted peaks at 284.8 eV, 285.6 eV, and 288.1 eV,

corresponding to C–C/C=C, C–O, and O–C=O bonds, respectively. In the detailed spectra of the O 1s, three types of O species, i.e., Metal-O, C=O, and C-O bonds, can be observed, which correspond to 530.1 eV, 531.7 eV, and 533.3 eV, respectively (Figure S8c). For the detailed Ni 2p XPS spectra of MHFs (Figure S8d), six fitted peaks at $[Ni^{2+}]$ = 73.2 mol% and eight fitted peaks at $[Ni^{2+}]$ = 100 mol% are observed. These peaks are related to diverse Ni species, including Ni^0 (853.0 and 870.2 eV), Ni^{2+} (855.7 and 873.4 eV), and satellite peaks (880.0 and 861.8 eV). When the $[Ni^{2+}]$ increases from 73.2 mol% to 100 mol%, the peak position shows a slightly negative shift, which could be primarily due to the metallic bond difference between metallic Ni and $Fe_{1-x}Ni_x$ alloys [17]. For the MHFs obtained at $[Ni^{2+}]$ = 0 mol%, six fitted peaks (Figure S8e) are observed to be associated with Fe^{2+} ions (710.5 and 723.9 eV), Fe^{3+} ions (712.1 and 725.6 eV), and satellite peaks (719.6 and 732.4 eV), indicating the presence of Fe_3O_4. After the addition of 73.2 mol% Ni^{2+} ions, two new peaks appear at 707.0 and 719.8 eV (Figure S8e), which are in relation to Fe^0. The XRD and EDX data demonstrate that the surfaces of $Fe_{1-x}Ni_x$ alloy foams have been oxidized into Fe/Ni species with high oxidation states in the air atmosphere.

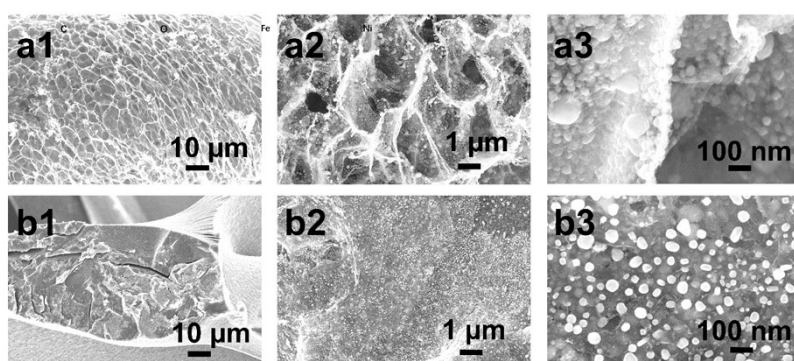**Figure S9** SEM images of the MHFs formed under diverse $[Ni^{2+}]$ (mol%): (a1–a3) 11.5 and (b1–b3) 91.3.
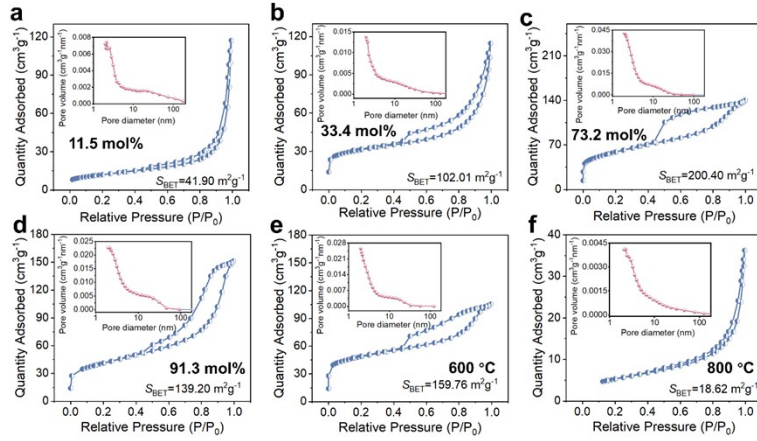
Figure S10 N_2 adsorption-desorption curves and (insets in a–d) the pore size distribution plots of MHFs formed under diverse (a–d) $[Ni^{2+}]$ (mol%) and (e–f) T_a.

Figure S11 The EMWAPs of MHFs formed under various $[Ni^{2+}]$ (mol%): (a1–c1) 3D RL plots, and (a2–c2) efficient absorption bandwidth (EABW, RL ≤ −10 dB) and the optimal ratio of bandwidth to thickness (EABW/d).

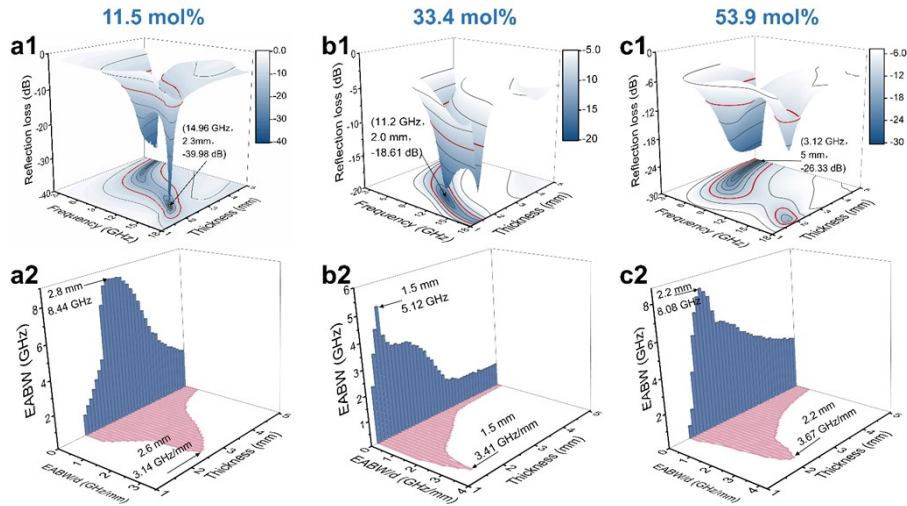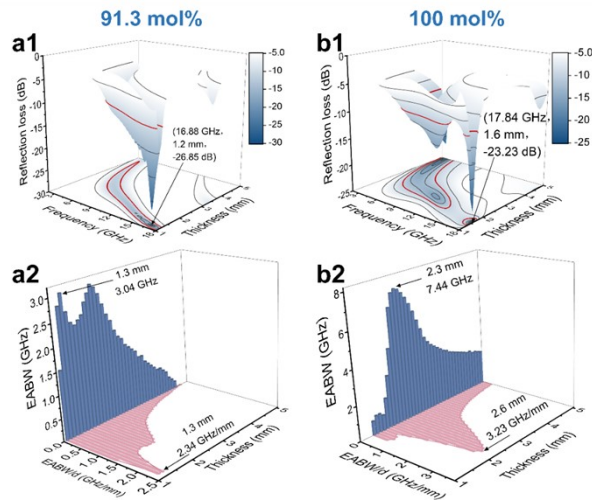**Figure S12** The EMWAPs of MHFs formed under various $[Ni^{2+}]$ (mol%): (a1–b1) 3D RL plots, and (a2–b2) efficient absorption bandwidth (EABW, RL ≤ −10 dB) and the optimal ratio of

bandwidth to thickness (EABW/d).
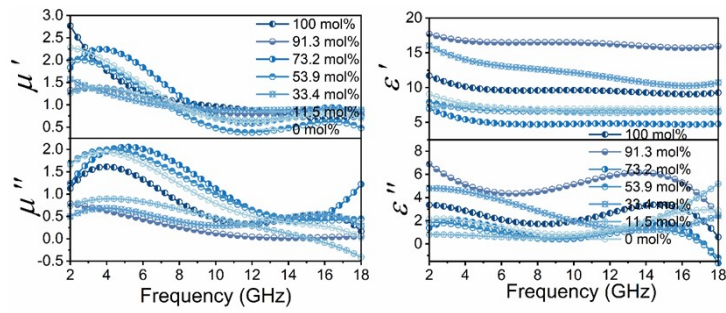
Figure S13 Electromagnetic parameter of MHFs/wax composites (50%) formed under various $[Ni^{2+}]$ (mol%): (a) the real and imagery of permeability and (b) the real and imagery of permittivity.
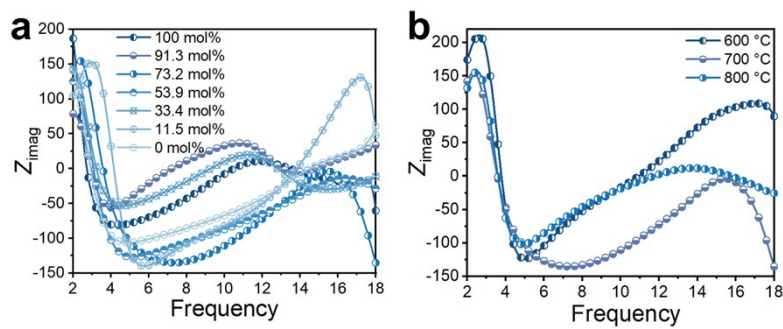
Figure S14 Z_{imag} of MHFs/wax composites (50%) formed under: (a) various $[Ni^{2+}]$ (mol%) and (b) diverse T_a.
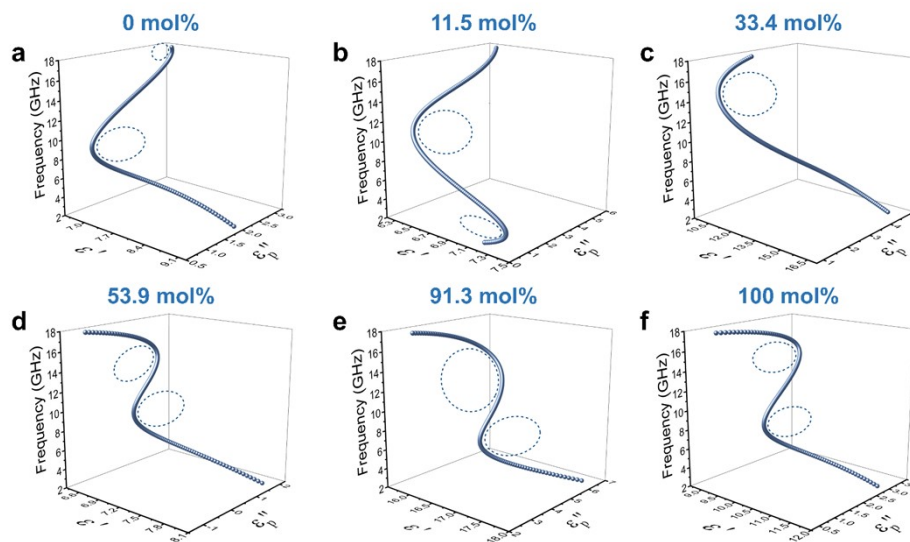
Figure S15 Cole-Cole plots of MHFs/wax composites (50%) formed under: (a) various $[Ni^{2+}]$ (mol%) and (b) diverse T_a.
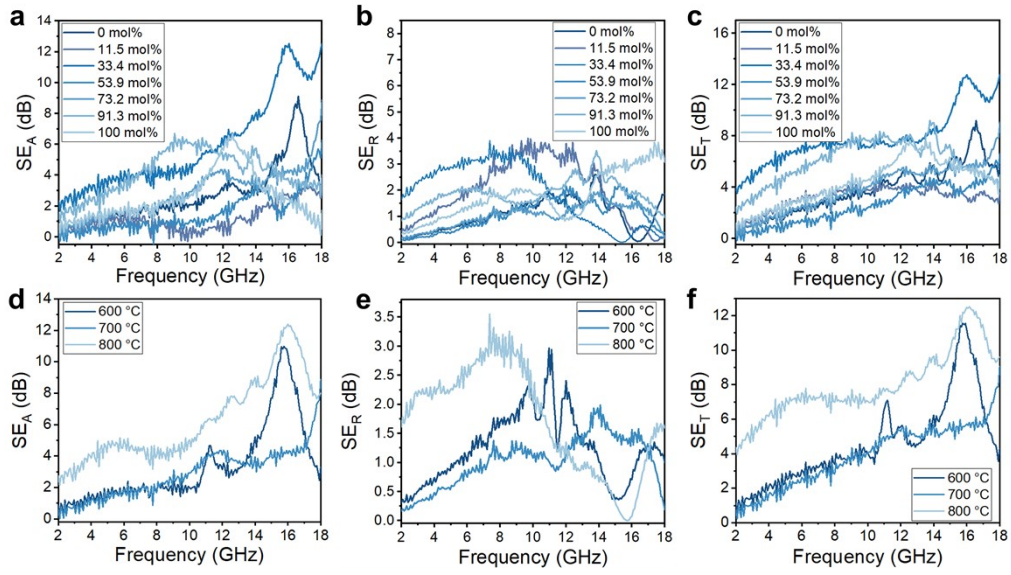
Figure S16 Influences of [Ni^{2+}] and T_a on (a, d) EMI SE$_A$, (b, e) EMI SE$_R$, and (b, e) total EMI SE$_T$ of the MHFs.
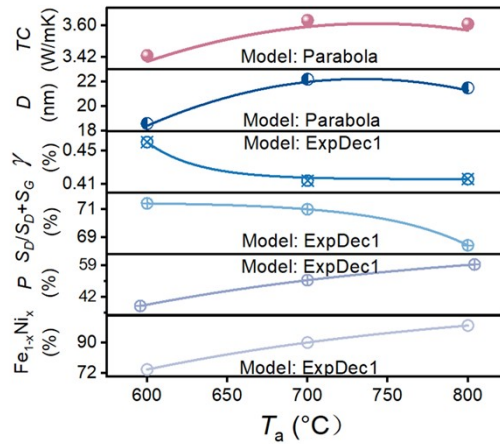
Figure S17 Variation tendency of S_{BET}, D, defects (γ, $CD\%$), P, Fe$_{1-x}$Ni$_x$ content, and TC with T_a.

Figure S18 (a) Test apparatus used for (b1–b7) the surface temperature as functions of heating and cooling time and the insets are Infrared thermal photos of MHFs produced under diverse [Ni^{2+}].

Table S1. EMWAP comparisons of magnetic composites with other absorbents.[19–37]

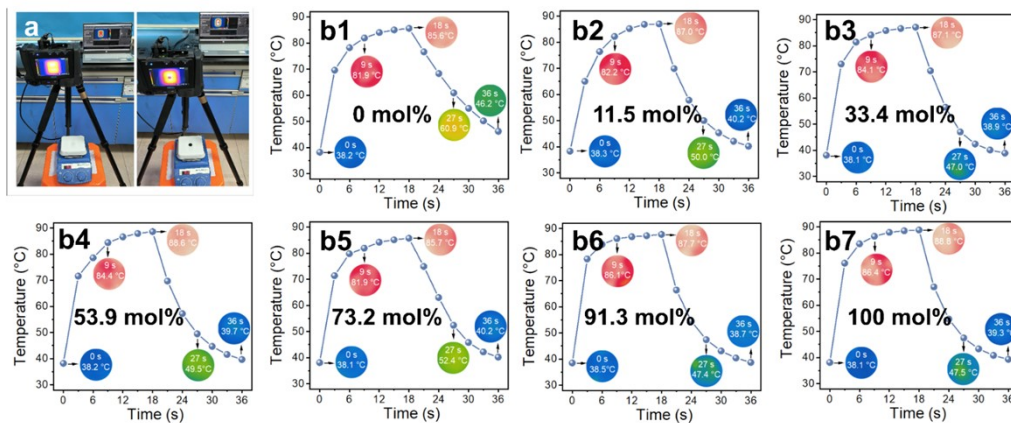| Specimens	Filling mass fraction (wt%)	RL$_{min}$ (dB)	f (GHz) (optimal R_L)	d (mm)	EAB (GHz) (RL ≤–10 dB)	ABW/d (GHz/mm)	Ref.
10% Ni-doped CeOHCO$_3$	50	−35.84	13.68	2.3	4.4	1.91	[19]
graphene/chiral PPy/Al$_2$O$_3$	55	−60.63	15.44	2.0	5.4	2.70	[20]
Fe$_3$O$_4$/C	60	−55.43	13.76	1.7	~4.7	2.76	[21]
FeSiAl/MgO	80	−21.55	12.84	1.5	5.25	3.50	[22]
Fe/MgO	96	−65.6	12.0	2.5	14.1	5.64	[23]
Co/C/Fe/C	40	-41.97	15.2	1.55	5.28	3.41	[24]
Ni/Co@C	40	-66.3 (2.0mm)	16.4	2.3	6.02	2.62	[25]
leaf-like Fe/C composites	60	-68.8 (3.25 mm)	5.4	1.5	6	4.00	[26]
Fe$_3$C/Fe/N-CNTs-800	15	-54.4 (2.3 mm)	10.4	1.55	4.3	2.77	[27]
carbon@Fe$_{20}$Ni$_{80}$	15	-39.5 (3 mm)	6.7	2.2	5.4	2.45	[28]
FeNi$_3$/N-GN	50	-57.2 (1.45 mm)	12.9	1.94	4.2	2.16	[29]
ZIF@NiFe-X	30	-59.5	16.61	2.06	7.23	3.50	[30]
H-Fe$_3$O$_4$@C	30	-58.44		1.9	6.0	3.16	[31]
Ni@C@ZnO	25	-55.8 (2.5 mm)	~10	2	4.1	2.05	[32]
FeNi@C-700	33	-30.4 (1.2 mm)	~17	1.4	4.6	3.28	[33]
FeNi@SnO$_2$	30	-49.1 (1.75 mm)	~13.1	1.75	6.76	3.86	[34]
10% Fe-doped CeOHCO$_3$	50	-47.22 (4.3 mm)	2.4	2.4	8.32	3.47	[19]
Fe@C@TiO$_2$@MoS$_2$	40	-54.2 (2.5 mm)	11.6	2.6	9.6	3.69	[35]
PPy/Fe$_3$O$_4$	30	-41.75 (2.3 mm)	9.52	2.1	10.24	4.88	[36]
Fe@SiO$_2$@C-Ni	80	-45.2 (3.3 mm)	7.5	3.3	13.1	3.97	[37]
100 mol%Ni-700°C	50	-23.23 (1.6 mm)	17.84	2.3	7.44	3.31	
91.3 mol%Ni-700°C	50	-26.85 (1.2 mm)	16.88	1.3	3.04	2.34	
73.2 mol%Ni-700°C	50	-48.72 (2.8 mm)	6.88	2.4	12.4	5.17	This work
53.9 mol%Ni-700°C	50	-26.33 (5.0 mm)	3.12	2.2	8.08	3.67	
33.4 mol%Ni-700°C	50	-18.61 (2.0 mm)	11.2	1.5	5.12	3.41	
11.5 mol%Ni-700°C	50	-39.98 (2.31 mm)	14.96	2.8	8.44	3.01	

0 mol%Ni-700°C	50	-25.39 (5.0 mm)	2.88	2.3	11.44	5.16

Table S2. Comprehensive comparison of the TC of 40 wt.% magnetic foam/silicone composites with other inorganic fillers.[15,16,38–53]

Filler	Matrix	Load (wt%)	Thermal conductivity (W/m·K)	Ref.
graphene/Cu-MgO	PCM salt	50	1.34	[38]
g-C$_3$N$_4$@Fe@C hollow micro-polyhedra	silicone	20	1.75	[39]
TiO$_2$/Fe/C nanocomposites	silicone	45	2.19	[40]
Ti$_3$C$_2$T$_x$ microflakes	silicone	50	2.75	[41]
Ti$_3$C$_2$T$_x$/(ANF@FeNi)		60	4.72	[42]
Fe-doped CeO$_2$/Ce(OH)$_3$ CSNFs	silicone	45	3.442	[15]
GPC	paraffin	90	0.58	[43]
CNF/Fe$_x$O$_y$	silicone	30	3.22	[16]
SA@PC/NRs	Stearic acid	42	0.81	[44]
γ-Al$_2$O$_3$@Ni@C	silicone	30	2.84	[45]
ER/3D-BP@Ni	epoxy resin	6.71 vol%	2.01	[46]
KF@PPy-Fe$_3$O$_4$/PW	paraffin wax	80	1.06	[47]
MWCNT-Fe$_3$O$_4$@Ag/epoxy	Epoxy	15	0.46	[48]
urchin-structured Fe$_3$O$_4$/carbon spine	PVDF	95	2.31	[49]
n-eicosane Fe$_3$O$_4$@SiO$_2$@Cu	/		1.30	[50]
MgO/Ni/MWCNT	silicone	40	3.61	[51]
EP/Cu NWs@Ni	epoxy	9 vol%	2.90	[52]
GO@Fe$_3$O$_4$@CF	epoxy	100	3.099	[53]
0 mol%Ni-700 °C	silicone	30	3.36	This work
11.5 mol%Ni-700 °C	silicone	30	3.58	
33.4 mol%Ni-700 °C	silicone	30	3.59	
53.9 mol%Ni-600 °C	silicone	30	3.43	
53.9 mol%Ni-700 °C	silicone	30	3.63	
53.9 mol%Ni-800 °C	silicone	30	3.61	
73.2 mol%Ni-700 °C	silicone	10	3.26	
	silicone	20	3.38	
	silicone	30	3.47	
	silicone	40	3.12	

91.3 mol%Ni-700 ℃	silicone	30	3.60	
100 mol%Ni-700 ℃	silicone	30	3.75	